Journal of
Materials Chemistry A

Highly Porous, Low Band-gap NixMn3-xO4 (0.55 ≤ x ≤ 1.2) Spinel Nanoparticles with In-situ Coated Carbon as Advanced Cathode Materials for Zinc-ion Batteries

Journal:	*Journal of Materials Chemistry A*
Manuscript ID	TA-ART-05-2019-005101.R1
Article Type:	Paper
Date Submitted by the Author:	26-Jun-2019
Complete List of Authors:	Long, Jun; College of Chemistry and Chemical Engineering, Central South University, Changsha 410083, PR China. , College of Chemistry and Chemical Engineering Gu, Jinxing; University of Puerto Rico, Rio Piedras Campus yang, zhanhong; Central South University Mao, Jianfeng; University of Wollongong, Hao, Junnan; University of Wollongong Chen, Zhongfang; University of Puerto Rico, Department of Chemistry Guo, Zaiping; University of Wollongong,

Title page

Title

Highly Porous, Low Band-gap $Ni_xMn_{3-x}O_4$ ($0.55 \leq x \leq 1.2$) Spinel Nanoparticles with In-situ Coated Carbon as Advanced Cathode Materials for Zinc-ion Batteries

Author names and affiliations

Jun Long[ab], Jinxing Gu[c], Zhanhong Yang[a]*, Jianfeng Mao[b], Junnan Hao[b], Zhongfang Chen[c]*, Zaiping Guo[bd]*

[a]Hunan Provincial Key Laboratory of Chemical Power Sources, College of Chemistry and Chemical Engineering, Central South University, Changsha 410083, P. R. China

[b]Institute for Superconducting & Electronic Materials, University of Wollongong, Wollongong, New South Wales 2522, Australia

[c]Department of Chemistry, Institute for Functional Nanomaterials, University of Puerto Rico Rio, Rio Piedras Campus, San Juan, PR 00931, USA.

[d]School of Mechanical, Materials, Mechatronics and Biomedical Engineering, University of Wollongong, Wollongong, New South Wales 2500, Australia

Electronic Supplementary Information (ESI) available: See DOI: 10.1039/x0xx00000x or from the author.

*Corresponding author:

Dr. & Prof. Zhanhong Yang. Email: zhyang@csu.edu.cn

Dr. & Prof. Zaiping Guo. Email: zguo@uow.edu.au

Dr. & Prof. Zhongfang Chen. Email: zhongfangchen@gmail.coom

Keywords

Zinc ion battery, Mn^{4+}-rich, Amorphous shell, Highly porous, Diffusion-controlled

Abstract

Aqueous Zinc ion batteries (ZIBs) are emerging as one highly promising alternative technology for grid-scale applications where high safety, environmental-friendliness, and high-specific capacities are needed. It remains a significant challenge, however, to develop a cathode with high rate capability and long-term cycling stability. Here, we demonstrate diffusion-controlled behavior in the intercalation of zinc ions in highly porous, Mn^{4+}-rich, and low-band-gap $Ni_xMn_{3-x}O_4$ nano-particles with carbon matrix formed in situ (with the composite denoted as $Ni_xMn_{3-x}O_4$@C, $x = 1$), which exhibits superior rate capability (139.7 and 98.5 mAh g^{-1} at 50 and 1,200 mA g^{-1}, respectively) and outstanding cycling stability (128.8 mAh g^{-1} remaining at 400 mA g^{-1} after 850 cycles). Based on the obtained experimental results and density functional theory (DFT) calculations, cation-site Ni substitution combined with enough doping concentration can decrease the band gap and effectively improve the electronic conductivity in the crystal. Furthermore, the amorphous carbon shell and highly porous Mn^{4+}-rich structure leads to fast electron transport and short Zn^{2+} diffusion paths in the mild aqueous electrolyte. This study provides an example of a technique for optimizing cathode materials for high-performance rechargeable ZIBs and designing advanced intercalation-type materials for other energy storage devices.

Introduction

Because our escalating population and energy production have been speeding up the combustion of fossil fuels [1] around the world, severe environmental issues have gradually appeared [2]. Therefore, the energy storage markets are flourishing in terms of their energy-saving technology and technical development [3, 4]. Furthermore, it is significant that the obtained energy should be produced from renewable energy resources and be stored [5-7] in effective ways. Environmentally friendly energy storage and conversion based on the electrochemical technology [8-13] can occupy a position of dominance in the energy market [14], because it can release/store energy with considerable conversion efficiency [15-20]. Lithium-ion batteries (LIBs) have been widely used in today's society because of their large specific power and high energy density [21-24]. The widespread use of LIBs to power portable electronic devices and for grid-scale energy storage could be impractical, however, because they are limited by their high cost [25, 26] and flammable electrolyte. Recently reported aqueous metal ion (monovalent-ion, bivalent-ion, multivalent-ion, etc.) batteries have garnered much attention owing to their high-energy-density, high-safety, and nontoxicity. Rechargeable aqueous zinc-ion batteries (ZIBs) [27-30] composed of an intercalation/deintercalation cathode, aqueous electrolyte, and zinc metal anode have become one of the most popular research hotspots in the energy and resources sector. Several advantages of ZIBs have already been demonstrated compared to LIBs and other nonaqueous metal ion batteries. Firstly, zinc offers important advantages over lithium due to its natural abundance and low cost, as well as its high theoretical specific capacity (820 mA h g^{-1}) and low working potential (-0.78 V vs. standard hydrogen electrode potential). Secondly, the processes of zinc deposition and stripping are also facile in aqueous electrolyte because of its high overpotential. Thirdly, the fewer safety concerns associated with ZIBs could make it possible to scale them up, due to their incombustibility and high volumetric capacity (5854 mA h/cm^{-3}) [31]. Many cathode materials for ZIBs have been reported so far, such as LiV_3O_8 [32], $Na_3V_2(PO_4)_3$ [30], MnO_2 [27], MnS [33], $ZnMn_2O_4$ [34], $Zn_3V_2O_7(OH)_2{\cdot}2H_2O$ [31], Prussian blue [35], etc. Despite these efforts, further scientific research into such excellent cathode materials with high capacity and remarkable cycling performance is essential, bearing in mind that ZIBs are just in the development stage.

Recalling the whole R&D process for Li-insertion cathodes, most previous studies have been focusing on the AMn_2O_4 (A= Zn, Co, Ni, etc.) spinel structure, which can improve the electrochemical performance compared to monovalent alternatives as well as the cycling stability [36, 37] because of the multiple Mn valences. Therefore, it is meaningful to explore these structures for Zn-storage. For example, the spinel structure of $ZnMn_2O_4$ [34] is maintained during the intercalation/de-intercalation process. $Zn(H_2O)_n^{2+}$ (zinc hydrated ions) cannot intercalate into the spinel structure. However, the H^+ can insert into the layered structure materials (such as MnO_2 and $NH_4V_4O_{10}$), and the OH^- react with $ZnSO_4$ and H_2O in the electrolyte to produce some large flake-like $ZnSO_4[Zn(OH)_2]_3{\bullet}xH_2O$ [27, 31]. Therefore, this phenomenon could increase the pH of the electrolyte. It can be concluded that the structure of the spinel systems is much more stable than the layered materials during the cycling. These Mn-based materials have common barriers to wider application, however, such as large volume variation and poor electrical conductivity during the phase transitions in the course of cycling. Among these systems (Mn-based electrodes) researched for energy storage, $NiMn_2O_4$, as one of the most interesting spinel oxides, was widely used in lithium-ion batteries (LIBs) and supercapacitors (SCs) with superior electrochemical activity and structural reversibility [38, 39] because of its synergetic Ni-Mn structure. Very recently, cation-site doping has been widely used to enhance its structural stability and intrinsic conductivity. $NiMn_2O_4$ can provide enough redox active sites [40] for the critical electrochemical reactions because of the lattice competition between nickel ions and manganese ions in the $NiMn_2O_4$ spinel metal oxide [41]. Furthermore, in contradistinction to other transition metal manganites (AMn_2O_4; A=Mg, Co, Fe, Mn, Zn), the crystalline structure of the Ni-Mn spinel is a symmetric cubic structure, which shows tetragonal distortion because of the dynamic Jahn-Teller effect [42] related to the existence of trivalent manganese in the octahedral sites. The tetrahedral lattice sites (A-sites) and the octahedral interstices (B-sites) are, respectively, occupied by divalent cations and trivalent cations for regular spinel [43-45]. Nevertheless, $NiMn_2O_4$ is not the usual type of spinel but a hybrid spinel, where a fraction y of the divalent nickel ions could leave the A-sites and are likely to be located on the B-sites in the crystal, which is characterized by a cubic close packing of oxygen atoms [42, 46-48]. This will result in a corresponding 2y of the trivalent manganese ions that is disproportionate to divalent manganese ions and tetravalent manganese ions in these B-sites, so that, simultaneously, the corresponding divalent manganese ions could migrate to the A-sites to balance the valence change brought by the transfer of divalent nickel ions [47]. This may result in capacity fading during cycling owing to the dissolution of Mn^{2+} for Mn-based materials. A Ni-doped electrode material with Mn^{4+}-rich phases can provide a much more flexible response to the active sites, however, optimizing the cycling stability and suppressing the destruction of crystal structure.

With these considerations from the above analysis in mind, new highly porous, narrow band-gap, and Mn^{4+}-rich $Ni_xMn_{3-x}O_4$ (x =0, 0.55, 0.8, 1.0, 1.2) nano-particles were synthesized in a carbon matrix formed in situ. The details are included in the experiment section in the Supporting Information. We report highly reversible Zn^{2+} de/intercalation and stable performance in the Zn/ $Ni_xMn_{3-x}O_4$@C system for the first time. The unique idea for the design could be principally demonstrated as follows: (Ⅰ) the Ni-doping endows the $Ni_xMn_{3-x}O_4$ with a low band-gap, improving its electrical conductivity; (Ⅱ) Ni-doped Mn^{4+}-rich $Ni_xMn_{3-x}O_4$ can provide much more flexible active sites to preserve the crystal structure; (Ⅲ) the pores inside $Ni_xMn_{3-x}O_4$ nanoparticles facilitate fast mass/ion transport and penetration in the mild electrolyte; (Ⅳ) the $Ni_xMn_{3-x}O_4$ in $Ni_xMn_{3-x}O_4$@C electrode could anchor the coated carbon strongly and conformally, restraining the aggregation and dissolution of $Ni_xMn_{3-x}O_4$. Based on these synergic effects, the Zn/ $Ni_xMn_{3-x}O_4$@C (x = 1) system can work well in aqueous electrolyte (2 M $ZnSO_4$ + 0.15 M $MnSO_4$), and demonstrate high specific capacity (133.7 m Ah g^{-1} at 200 mA g^{-1}), long-term cyclability (91.9% capacity retention after 850 cycles at 400 m A g^{-1}) in the range of 1.0-1.85 V. Its electrochemical properties can be improved by designing the mole ratio of Ni and Mn, owing to the displacement of Ni^{2+} from B sites, which can change the electrical properties introduced by the “hopping mechanism” on B-sites of Mn^{3+} and Mn^{4+} via localized states [48, 49-50]. Moreover, the mechanism of Zn^{2+} de/intercalation in nonstoichiometric $Ni_xMn_{3-x}O_4$ spinel coated in situ by amorphous carbon layers has been deeply studied by ex situ X-ray diffraction (XRD), X-ray photoelectron spectroscopy (XPS), scanning electron microscopy (SEM), energy-dispersive spectrometry (EDS), transmission electron microscopy (TEM), first-principles calculations, and nitrogen adsorption/desorption experiments.

Results and Discussion

Structure Characterization

As shown in Figure 1a, the synthesis of $Ni_xMn_{3-x}O_4$@C samples with different Ni: Mn ratios was confirmed by powder XRD analysis. The obtained XRD data as a function of the Ni proportion in a series of prepared samples correspond well to the $NiMn_2O_4$ spinel structure (Fd3m), which indicates that the calcination of precursors did not change the crystal structure of $Ni_xMn_{3-x}O_4$@C. For these $Ni_xMn_{3-x}O_4$@C hybrids, no NiO impurity was detectable except for the $Ni_xMn_{3-x}O_4$@C (x = 1.2) composition, demonstrating the successful transformation of the $Ni_xMn_{3-x}O_4$@C (x = 0.55, 0.8, 1), which was understood by reference to the JCPDS standard. Interestingly, when the Ni content was increased from 0 to 0.55, 0.85 and 1, respectively, $Ni_xMn_{3-x}O_4$@C (x = 0) with the tetragonal Mn_3O_4 (JCPDS, 24-0734, I41/amd) structure (as shown in Figure S1 in the Supporting Information) was gradually transformed into $Ni_xMn_{3-x}O_4$@C (x =1) with the space group Fd3m. Compared with $Ni_xMn_{3-x}O_4$@C (x = 0.55, 0.8), the strong peaks of $Ni_xMn_{3-x}O_4$@C (x =1) composition at 2θ = 18.3°, 30.15°, 34.95°, 36.86°, 43.52°, 53.54°, 57.90°, 62.95°, 73.99°, and 75.37° correspond to the reflections of (111), (220), (311), (222), (400), (442), (511), (440), (533), and (622) in the XRD standard of $NiMn_2O_4$ (JCPDS, 1-1110, Fd3m). It has been found, however, that the peaks of NiO (JCPDS, 47-1049, Fm-3m (225)) were only observed in the $Ni_xMn_{3-x}O_4$@C ($x = 1.2$) sample, which are labeled with blue stars. This is due to the fact that further increase of Ni content to 1.2 could lead to segregation of multiphase materials including NiO and Ni_2MnO_4, which indicates that substitution limit of Ni for Mn in the $Ni_xMn_{3-x}O_4$@C ($x = 1.2$) has been reached. We find that nearly all of the peaks of the samples are shifted to lower 2θ values, especially between the dashed-dotted lines, denoting a larger lattice constant with increasing the Ni content. The peaks in Figure 1a are known to shift to lower 2θ values with the substitution of large radius foreign ions [51]. The ionic radius of Ni^{2+} (69 pm) is larger than that of Mn^{2+} (60 pm), Mn^{3+} (58 pm), and Mn^{4+}(53 pm), consistent with this trend.

To discern the positions of Ni and Mn ions in the lattice interstices, the intensity ratio $R=I_{400}/I_{220}$ can be used to study the distribution between them in AB_2O_4 spinels [44], and it has been reported that the value of R could change if an increasing proportion of foreign ions are substituted at A-sites. Furthermore, the XRD pattern of $Ni_xMn_{3-x}O_4$@C ($x = 0$) was also obtained, as shown in Figure S1 as a comparison. In the case of $Ni_xMn_{3-x}O_4$@C ($x = 0$), the obtained R is 1.237. The values of R measured for $Ni_xMn_{3-x}O_4$@C ($x = 0.55, 0.8, 1$) are 1.228, 1.230 and 1.235, respectively, which indicates that an increasing proportion of Ni^{2+} is likely to be occupying B-sites, substitutions that prefer to occupy Mn-sites instead [47]. This will be further studied by means of density functional theory (DFT). In Figure S1, however, all characteristic peaks are indexed to the tetragonal spinel structure of Mn_3O_4 with space group I41/amd. In this structure, the Mn^{2+} preferentially occupies A-sites, while Mn^{3+} occupies the B-sites. It is interesting to note that the valence of Mn in Mn_3O_4 may be not the same as that exhibited in $Ni_xMn_{3-x}O_4$@C. The substitution of Ni on the B-sites of Mn_3O_4 could change the valence state of Mn owing to the electroneutrality principle [47]. A similar phenomenon has been reported in a previous reference [52] on the substituted $LiM_xMn_{2-x}O_4$ (M= Cr, Li, Ni, etc.) spinels.

More importantly, Ni cations in spinels enhanced cycling capacities [21] in $Li(Ni_yMn_zCo_{1-x-y})O_2$ cathodes for LIBs, and Mn cations stabilized the spinel structure after partial substitution by Ni cations at B-sites. It is noteworthy that cations with a larger ionic radius and lower valence can balance the crystal stress and stabilize the spinel structure if they coexist with other cations with a smaller radius and higher valence state at the B-sites. For example, cooperative synergies between nickel cations (+2) and manganese cations (+4) made it possible to increase the stability [53] of the framework of $LiNi_{1/3}Co_{1/3}Mn_{1/3}$ during charge-discharge cycling.

XPS measurements were carried out to evaluate the oxidation states of Mn and Ni cations in $Ni_xMn_{3-x}O_4$ and $Ni_xMn_{3-x}O_4$@C (x = 1), and the corresponding survey spectra are shown in Figure S2 and Figure 1b. Figure 1b demonstrates the existence of signals associated with Ni, Mn, O, and C. The Ni: Mn ratio (1 :2.002) was also obtained according to the integrated intensity of the corresponding peaks, which were corrected by the elemental sensitivity factors. The result from XPS may not be completely dependable, because it is a semi-quantitative method. The obtained Ni/Mn atomic ratio, which is close to the designed value for the experiment, indicates, however, that Ni and Mn cations are homogeneously distributed within the limits of the XPS analytical depth. Ni 2p and Mn $2p_{3/2}$ photoemission spectra are shown in Figure 1c and Figure 1d, respectively. In the case of Ni 2p, the spectrum shows the presence of two main peaks at 854.2 eV ($2p_{3/2}$) and 871.9 eV ($2p_{1/2}$) along with two satellite peaks at 860.8 eV and 878.8 eV. Interestingly, the peak distance between the satellites and the main peaks is about 7 eV, whereas the main peak difference is 17.7 eV, similar to the value of 17.6 eV observed for Ni^{2+} [54] in NiO. The large full-width half-maxima (FWHM) for Mn $2p_{3/2}$ signals of $Ni_xMn_{3-x}O_4$@C ($x = 1$) is indicative of multiplet splitting along with the charging effect [46], owing to the presence of Mn^{4+}, Mn^{3+} and Mn^{2+} ions. The Mn$2p_{3/2}$ spectrum of $Ni_xMn_{3-x}O_4$@C (x = 1) composites is a superimposition of Mn^{4+}, Mn^{3+}, and Mn^{2+} peaks, as shown in the Figure 1d, demonstrating that Mn occurs in three different oxidation states. These peaks correspond with binding energy of 643.5 eV, 642.4 eV, and 641.5 eV [46], respectively. It was observed that the peak area belonging to Mn^{4+} is the largest among them from the results of XPS investigations of the $Ni_xMn_{3-x}O_4$@C ($x = 1$) compound (Table S1, Supporting Information). Why do we choose it as the example for further study? The $Ni_xMn_{3-x}O_4$@C ($x = 1$) exhibits fine and stable crystal structure according to the physical characterization, shows a highly Mn^{4+}-rich structure, and displays good morphology with uniform nanoparticles, proved below. Furthermore, the as-prepared $Ni_xMn_{3-x}O_4$@C ($x = 1$) has highest content of Mn^{4+} (as shown in Figure S3) in its crystal structure after the precursor is calcined at the target temperature of 455

^{o}C for 2.5 h in oxygen atmosphere. The O 1s spectrum of $Ni_xMn_{3-x}O_4$@C (x = 1) is deconvoluted into three peaks in Figure 1e, where the peak at 529.9 eV (O1) is due to the metal oxygen bonds, whereas a weaker peak at 531.5 e V (O2) is correlated with the large amount of -OH species adsorbed on the surface. The smallest peak at 533.2 eV (O3) could be due to chemisorbed oxygen or adsorbed water at the surface of the sample. The core-level XPS spectrum of C 1s for $Ni_xMn_{3-x}O_4$@C ($x = 1$) consists of three components centered at 284.8 eV, 286.1 eV and 288.3 eV, corresponding to the C-C, C-O, and C=O bonds, respectively (Figure 1f).

From these XPS results, the valence of Mn ion could change [46, 47] during the Ni substitution for Mn in the $Ni_xMn_{3-x}O_4$ structure, which is consistent with the previous discussion. Additionally, Mn^{4+} displays a higher valence than Mn^{3+} but a smaller ionic radius, while the Ni^{2+} exhibits a lower valence than Mn^{3+} but a larger ionic radius. The substitution of Ni species [9] in the crystal structure has been proven to boost the reversible capacity, while Mn species ameliorate the interfacial impedance [1] and enhance the electrochemical performance. Therefore, the synergies between the Ni^{2+} and Mn^{4+} and their cosubstitution of Mn^{4+}-Ni^{2+} for Mn^{3+} balance the valence charge at B-sites in the crystal lattices, which relieves the crystal stress owing to the mismatching ionic radius and hence promotes the stability of the spinel structure. Furthermore, the Mn^{4+} rich phase in $Ni_xMn_{3-x}O_4$@C ($x = 1$) can act as protective component to improve the medium for more diffusing zinc ions and alleviating the Mn^{2+} dissolution during charge-discharge. According to above-mentioned research results, it has been observed that the intensively synergic action between Ni^{2+} and Mn^{4+} at B-sites —could be used as the evidence for the reversibility and stability of the active materials during charge/discharge. Furthermore, more details on the changes to the microstructure and the lattice defects of the obtained samples were also revealed by Raman spectroscopy (Figure S4**)** and Fourier transform infrared (FTIR) spectroscopy (in Figure S5), which are complementary and provide valuable information on the chemical bonds information in Ni-Mn-O systems in the hybrids.

It can be seen from the Raman spectra (in Figure S4) of $Ni_xMn_{3-x}O_4$@C hybrids that the intense vibrational modes located around 654 cm^{-1} and 556 cm^{-1} are assigned as the A_{1g} and F_{2g} modes, respectively. The peak located at 556 cm^{-1} reflects the symmetric Ni-O stretching vibration derived from F_{2g} mode [55] in $NiMn_2O_4$. The A_{1g} active mode originates from the symmetric Mn^{4+}-O (MnO_6) stretching vibration at octahedral sites [56]. Interestingly, the Mn^{2+}-O and Mn^{4+}-O vibrations at A-sites and B-sites are in accordance with the results obtained from the XRD and XPS analysis above. Additionally, the T_{2g} (located at 305 cm^{-1}) and E_g (located at 372 cm^{-1}) modes gradually disappear as x increases in the $Ni_xMn_{3-x}O_4$@C compounds, and the F_{2g} and Ni-O (locates at 509 cm^{-1}) stretching modes appear. These results indicate that Mn^{3+}-O is transformed into Mn^{4+}-O at the B-sites during the Ni substitution for Mn in the $Ni_xMn_{3-x}O_4$ structure. Typical carbon peaks located at 1362 cm^{-1} (D band) and 1580 cm^{-1} (G band) are detected from the samples. Furthermore, Fourier transform infrared (FTIR) spectroscopy is a complementary characterization method, which provides valuable information of Ni-Mn-O systems. The absorption peaks at 597 cm^{-1} and 507 cm^{-1} are assigned to Mn-O_4 and Mn-O_6 [56] vibrations (Figure S5), respectively, and the lower absorption bands at 452 cm^{-1} can be assigned to Ni-O$_6$, indicating that Ni can substitute for Mn at B-sites along with the change in the valence of Mn^{3+} at the B-sites. It should be noted that Mn^{4+} and Ni^{2+} at the B-sites take the place of Mn^{3+} in the compounds, as evidenced by the analysis of XRD, XPS, Raman spectroscopy, and FTIR spectroscopy. The overall typical nanoparticle morphologies of the as-prepared $Ni_xMn_{3-x}O_4$@C compounds and their crystal phases were characterized by using SEM, selected-area electron diffraction (SAED) analysis, energy dispersive X-ray spectroscopy (EDX) elemental mapping, and high resolution TEM (HRTEM) (as shown in Figure 2 and Figure S6). The samples show an irregular particle morphology with the size range of 15-25 nm (Figure 2a-2c), and the morphology is transformed into more irregular aggregated rectangular bulks (Figure 2d) on a large scale (x = 1.20), indicating that insufficient or excess content of Ni in the $Ni_xMn_{3-x}O_4$@C compounds can affect morphology of the nanoparticles. Therefore, high-resolution TEM and low-resolution TEM images (Figure 2g and its inset) of $Ni_xMn_{3-x}O_4$@C (x = 1.2) reveal various aggregates with mixed phases. The lattice spacings measured in Figure 2g shows interplanar spacings of 0.241 nm and 0.207 nm corresponding to the (1 1 1) and (2 0 0) planes of crystalline NiO, which are consistent with the XRD (Figure 1) and SAED (Figure S6b) results. Furthermore, the EDX spectrum (Figure S6a) demonstrates that the ratio of Ni: Mn is 1: 2.026 in $Ni_xMn_{3-x}O_4$@C (x = 1), whereas the ratio of Ni: Mn is 1:2.002 according to inductively coupled plasma – atomic emission spectrometry (ICP-AES) results. The differences between these two values and the theoretical ratio are quite small, further demonstrating the successful substitution of Ni for Mn.

Elemental mapping images (Figure 2i-i_4) of C, Ni, Mn, and O manifest no distinct phase segregation, revealing a homogeneous distribution of Ni and Mn elements in the $Ni_xMn_{3-x}O_4$@C ($x = 1$) hybrid. The diffraction rings obtained from the SAED (inset of Figure 2e) characterization indicate the polycrystalline nature of this sample. The HRTEM lattice image of this compound is also shown in Figure 2f, which displays well-defined crystalline planes with d-spacings of 0.483 nm and 0.296 nm, corresponding to the (1 1 1) and (2 2 0) lattice planes of face-centred cubic spinel (Fd3m) phase, respectively. As seen in Figure 2e and Figure 2f, there is a thin amorphous carbon layer (~ 2 nm) coated on the surface of $Ni_xMn_{3-x}O_4$@C ($x = 1$), which can be conductive to restraining the aggregation and volume changes of $Ni_xMn_{3-x}O_4$@C ($x = 1$) nanocrystals during charge/discharge and improving the conductivity of the electrode. The weight percentage of the carbon (9.8 wt%) was determined by thermogravimetric (TG) analysis, as shown in Figure S7. Additionally, the mesoporous structure of the $Ni_xMn_{3-x}O_4$@C ($x = 1$) compound is confirmed by an obvious hysteresis loop (Figure S6c) in the N_2 adsorption-desorption isotherms, proving a large surface area of 75.275 m^2 g^{-1} and a wide pore-size distribution at ~4.76 nm (The pore volume is calculated to be ~0.39 cm^3 g^{-1}.)

Electrochemical Performance

We investigated the electrochemical properties of the $Ni_xMn_{3-x}O_4$@C samples using typical coin cells, employing Zn foil anode, glass fiber separator, and aqueous electrolyte (2 M $ZnSO_4$ + 0.15 M $MnSO_4$), and a schematic illustration of the ZIB is presented in Figure 3a. Enlargements of the cathode and the interior of $Ni_xMn_{3-x}O_4$@C

(x = 1) are shown in Figure 3b and Figure 3c, respectively. The $Ni_xMn_{3-x}O_4$ inside the nano-particles generates numerous narrow pores so that zinc ions could transfer more efficiently through these tunnels (Figure 3d). The uniquely designed $Ni_xMn_{3-x}O_4$@C (x = 1) with its spinel structure and conductive carbon network provides superior electrochemical performance. Figure 3e displays the possible reaction mechanism of zinc ion intercalation/deintercalation in the $Ni_xMn_{3-x}O_4$@C (x = 1). Figure 4a shows the cyclic voltammetry (CV) curves of $Ni_xMn_{3-x}O_4$@C (x = 1) measured between 1.0 and 1.85 V within the first eleven cycles at a scan rate of 0.3 mV s^{-1}. The profiles in the first and third cycles are slightly shifted to higher potentials in comparison with the following cycles, which can be related to the initial activation of the electrode. During cycling, the polarization of the electrode decreases from the third cycle, as demonstrated (in Figure S8) by the electrochemical impedance spectroscopy (EIS) analysis. The CV curves (Figure 4a) prove that there is only one pair of redox peaks for $Ni_xMn_{3-x}O_4$@C (x = 1) at about 1.34/1.52 V during subsequent cycles, which can be attributed to the Zn^{2+} deintercalation/intercalation from/into the host, and which are consistent with the voltage plateaus shown in the charge and discharge curves (Figure 4b). The first discharge plateau at about 1.30 V corresponds to Zn^{2+} intercalation into the cathode, while the first charge plateau at about 1.55 V originates from Zn^{2+} extraction. The pair of redox peaks $Ni_xMn_{3-x}O_4$@C (x = 1) at 1.34/1.52 V could be owing to the reversible conversion of Mn^{3+}/Mn^{4+}, which can be attributed to the corresponding phase transition during charge/discharge. The charge storage kinetics and the phase transition in the $Ni_xMn_{3-x}O_4$@C (x = 1) host will be below.

As expected, the possible cathodic process may proceed as follows:

$$Ni_xMn_{3-x}O_4 + yZn^{2+} + 2ye^- \longleftrightarrow Zn_yNi_xMn_{3-x}O_4 \qquad (1)$$

Furthermore, the CV data indicate little change in potential or peak area loss after the third cycle for all the redox features, proving that $Ni_xMn_{3-x}O_4$@C ($x = 1$) can be an appropriate cathode candidate for aqueous ZIBs.

Figure 4b presents the discharge/charge curves of $Ni_xMn_{3-x}O_4$@C ($x = 1$) electrode cycled at the current density of 150 mA g^{-1} within the voltage window of 1.0-1.85 V. The active material delivers initial specific discharge and charge capacities of 115 mAh g^{-1} and 119 mAh g^{-1}, respectively. After 100 cycles, the electrode sustains stable capacity of around 130 mAh g^{-1} with high coulombic efficiency (CE) of around 100%. The average discharge plateau is 1.37 V during cycling, giving an excellent energy density of ~178.1 Wh kg^{-1} according to the active mass. The $Ni_xMn_{3-x}O_4$@C ($x = 1$) nanoparticles can provide a calculated energy density of 67 Wh kg^{-1} on the condition that the content of cathode materials occupies one third of the whole weight of the battery, which is much higher than for Ni-Cd (about 50 Wh kg^{-1}) and Pb-acid (about 30 Wh kg^{-1}) batteries. In comparison, a $Ni_xMn_{3-x}O_4$ + C (x = 1) mixture (9.8 wt % carbon) displays an obviously lower capacity of 44 mAh g^{-1} at 100 m A g^{-1} after 100 cycles (Figure S9). To evaluate the capacity from the carbon layer coated in situ on the surface of $Ni_xMn_{3-x}O_4$@C ($x = 1$), galvanostatic charge/ discharge curves (Figure S10) of the carbon matrix synthesized by the same method were collected between 1.0 and 1.85 V at 15 mA g^{-1} and indicate that the obtained capacity (~0.5 mAh g^{-1}) can be neglected.

Figure 4d presents the cycling performances of the obtained samples at 250 mA g^{-1} over 400 cycles. All the samples clearly display a gradual capacity increase before 53 cycles owing to the process of electrochemical activation. The capacity of $Ni_xMn_{3-x}O_4$@C (x = 0, 0.55) began to drop quickly after electrochemical activation, however, and their capacity retention ratios are 45% and 48% after 400 cycles, respectively, representing bad electrochemical performance. The $Ni_xMn_{3-x}O_4$@C (x = 1, 1.2) composites with enough Ni substitution present better cycling stability than the samples with less Ni content, mainly due to the mount of Ni in the composites, which can affect the crystalline structure of $Ni_xMn_{3-x}O_4$, as discussed in section 2.1. The discharge capacity of $Ni_xMn_{3-x}O_4$@C (x = 1) is the highest (130 mAh g^{-1} after 400 cycles) among them with a shortened activitation process, indicating enhanced Zn^{2+} deintercalation/intercalation kinetics. These excellent cycling performances could be principally due to several factors. First, the characteristic inverse spinel structure with abundant porosity and Mn^{4+}-rich crystalline phase could provide countless bonding sites and shorten the Zn^{2+} ion diffusion paths. Second, the moderate amounts of Mn^{2+} in the electrolyte efficiently suppress the structural collapse of $Ni_xMn_{3-x}O_4$, which can enhance the cycling stability and diminish the deterioration of the electrochemical performance (as shown in Figure S11). Third, the homogeneous in-situ carbon coating can enhance the ionic and electronic conductivities and increase cycling stability. The impressive zinc ion storage performance of $Ni_xMn_{3-x}O_4$@C (x = 1) is further emphasized by its excellent rate capability. Figure 4e presents the rate performance at different current densities, and the corresponding cycle profiles are shown in Figure 4c.

The cell displays reversible discharge capacity (130 mAh g^{-1}) at the current density of 400 mA g^{-1}, which is close to the achieved discharge capacity (139 mAh g^{-1}) at lower current density of 50 mA g^{-1}. It should be noted that the obtained capacities from 50 mA g^{-1} to 100 mA g^{-1} are nearly invariable. This similarity in capacity demonstrate that 139.7 mAh g^{-1} is the limit for the deintercalation/intercalation of zinc ions from/into the $Ni_xMn_{3-x}O_4$@C ($x = 1$) hybrids. As the current density increases to 600 mA g^{-1}, 800 mA g^{-1}, 1000 mA g^{-1}, and 1200 mA g^{-1}, the reversible capacity progressively decreases to 90%, 85%, 79%, and 68%, respectively. The capacity fading (in Figure 4e) is not irreversible when the cell is cycled at 1200 mA g^{-1}, because it can recover the previous capacity when subsequently cycled at a current density of 200 mA g^{-1}. The rate performance of $Ni_xMn_{3-x}O_4$@C ($x = 1$) is superior to those of the other samples, as confirmed in Figure S12. Moreover, the $Ni_xMn_{3-x}O_4$@C ($x = 1$) electrode could operate for more than 200 cycles with a high reversible capacity (nearly ~97% recovery of capacity) of 131 mAh g^{-1} after the rate test. The long cycling stability of $Ni_xMn_{3-x}O_4$@C ($x = 1$) was further investigated at 400 mA g^{-1} over 850 cycles. As can be seen in Figure 4f, the reversible capacity is 129.5 mAh g^{-1} after dozens of cycles of activation and remains stable in the subsequent cycles, demonstrating superior cycling stability. Furthermore, the coulombic efficiency was increased significantly to 97.8% after about 35 cycles, and then it reaches almost 100% subsequently. The typical plateaus and shapes of the discharge/charge profiles of $Ni_xMn_{3-x}O_4$@C ($x = 1$) at 400 mA g^{-1} were also recorded after different cycles (Figure S13), further manifesting its superb cycling stability. Compared with the reported cathode materials (in Table S2) and other Mn-based materials (in Figure S14), it shows remarkable cycling stability.

Zn Intercalation Mechanism

Structural studies and electrochemical investigation were used to further understand the de/intercalation mechanism and storage behavior of the $Ni_xMn_{3-x}O_4$@C electrodes. Ex-situ XPS (Figure S15a and Figure S15b) and XRD measurements (Figure 5a and Figure 5b) were carried out to analyze the mechanism of zinc ions de/intercalation from/into the $Ni_xMn_{3-x}O_4$@C ($x = 1$) host. The ex-situ XRD study was conducted in the range from 15° to 77° during the first cycle in ZIBs. All the peaks could be indexed to the $Ni_xMn_{3-x}O_4$ structure for the pristine electrode. The (1 1 1), (2 2 0), (5 1 1), and (4 4 0) peaks in the patterns display an obvious shift to lower 2θ angles during discharge and return to their original positions in the following charge, which can be attributed to more zinc ions being extracted/inserted within the tested voltage range. Furthermore, some additional peaks, except for those for the current collector, emerge in the subsequent de/intercalation, in the potential region where the $Ni_xMn_{3-x}O_4$@C ($x = 1$) host was intercalated by plenty of zinc ions. During the first discharge platform above 1.35 V, only two sets of peaks exist, which are related to the pristine $Ni_xMn_{3-x}O_4$@C ($x = 1$) and the steel current collector. Subsequently, some new peaks rose gradually and the peaks of $Ni_xMn_{3-x}O_4$@C ($x = 1$) decreased during the following discharge process. The new peaks began to diminish and disappear little by little, while the peaks of $Ni_xMn_{3-x}O_4$@C ($x = 1$) recovered to the original pattern during the subsequent charge process, demonstrating the excellent structural stability of $Ni_xMn_{3-x}O_4$@C ($x = 1$) nano-composite. We note that a small amount of Mn ions shifted to A-sites from B-sites, leading to some Mn-associated vacancies, which may induce some zinc ion diffusion along with the consequent structural transformation in the voltage range of about 1.4-1.0 V during discharge/charge. The crystal structure of the active materials can be preserved, however, because of the synergetic effects of Mn^{2+} and Zn^{2+} in the electrolyte, indicating the significantly reversible behavior of $Ni_xMn_{3-x}O_4$@C ($x = 1$). Good reversibility of zinc stripping/plating (Figure S16a and S16b) can be observed for the Zn^{2+} electrolyte with Mn^{2+} additive, which showed a decrease of overpotential during cycling. In addition, the peak positions for the intermediate transition phase (rich in zinc ions) can be indexed to nickel zinc manganite spinel structure, $(Zn_{0.988}Mn_{0.012})(Mn_{1.326}Zn_{0.024}Ni_{0.65})O_4$ (JCPDS No. 04-01-070-6709). As shown in Figure S15b, the intensity of Zn_{2p} in the discharge states is far above that at the charge states, further manifesting the intercalation/deintercalation of zinc ions into/from the Mn^{4+}-rich host. The zinc signal in Figure S15b did not disappear completely, which can attribute to the residual Zn^{2+} (on the surface of host) from the electrolyte. Moreover, the CV curves at various scan rates after activation at a scan rate of 0.2 mV s^{-1} for three cycles are presented in Figure 5c. Obviously, the peaks gradually grow broad and high with increasing scan rate, but the shapes of the obtained CV curves remain consistent. As assumed, only one pair of redox peaks could be detected at scan rate from 0.4 to 1.8 mV s^{-1} within the range of 1.0-1.85 V for each CV curve, which ought to be attributed to the Mn^{4+}/Mn^{3+} redox couple reactions, together with Zn^{2+} insertion/ extraction step by step into/from the tetrahedral sites of the $Ni_xMn_{3-x}O_4$@C (x = 1) framework. XPS spectra of the O 1s and Mn 3s orbitals for $Ni_xMn_{3-x}O_4$@C (x =1) were tested after discharge/ charge. As can be seen from Figure S17a, the O 1s XPS spectra for $Ni_xMn_{3-x}O_4$@C (x =1) are different between the charge state and the discharge state, while the positive shift of the stronger peak at 530.1 eV can be attributed to the intercalation of Zn^{2+} into the sample during discharge. The Mn 3s spectra (Figure S17b) contain two peaks, which are separated by 5.2 eV after discharge [57], indicating the reduction of Mn^{4+} to Mn^{3+}. The Mn 3s spectra also contain two peaks that are separated by 4.7 eV after charge, which reflects the Mn^{3+} to Mn^{4+} [58] and the extraction of Zn^{2+} from the sample. Therefore, it is reasonable to assume that the spinel host can support a zinc-rich and a zinc-depleted state without obvious polarization during the electrochemical processes for the electrode between 1.0 and 1.85 V, indicating good reversibility and excellent cycling stability. To obtain further insight into the zinc-storage mechanisms of the electrode, kinetic analysis according to the scan rate CV curves was carried out to research the contributions to the capacity of the diffusion-controlled and the capacitive controlled processes. The relationships between the scan rate (v) and the measured peak current (i) are shown in Figure 5d, which can be depicted as in the following equation:

$$i = av^{b} \qquad (2)$$

where a and b are adjustable parameters, and the b-values can be obtained from calculation of the slope of the plot (log i versus log v), which can be described as follows:

$$\log i = \log a + b \log v \qquad (3)$$

In particular, the b-value can vary between 0.5 and 1.0 under well-defined conditions. The b-value of 0.5 demonstrates completely diffusion-dominated intercalation behavior, while the b-value of 1.0 indicates a typical capacitive process. The b-values of 0.53 for anodic peaks and 0.55 for cathodic peaks can be matched at the scan rate from 0.4 to 1.8 mV s^{-1}, manifesting the kinetics of a diffusion-controlled process. In addition, the charge-transfer resistance (~109 Ω) of $Ni_xMn_{3-x}O_4$@C ($x = 1$) is somewhat lower than for the other samples after 100 cycles at 250 mA g^{-1}, as shown in Figure S18, indicating higher electrical conductivity. CV measurements using the three-electrode system were conducted. Notably, the aqueous electrolyte (2 M $ZnSO_4$ + 0.15 M $MnSO_4$) supports a wide electrochemical window as shown in Figure S19, and the O_2 evolution was suppressed significantly up to 2.15 V.

In order to further prove the relationship between electrical conductivity and the mount of Ni substitution on B-sites, the projected density of states (PDOS) of $Ni_xMn_{3-x}O_4$ were calculated. Clearly, Figure 5e$_{1-4}$ displays the unit cells of the pure Mn_3O_4 and other $Ni_xMn_{3-x}O_4$ materials, where the pure Mn_3O_4 has a spinel structure, which belongs to the I41/amd space group because of the Jahn-Teller distortion effect, while according to our experiments, Ni doped Mn_3O_4 has the space group Fd-3m. To simulate $Ni_xMn_{3-x}O_4$ with various Ni concentrations, we chose the Fd3m unit cell containing six Mn atoms. Various values of x (0.55, 0.80, 1.00, 1.20) in $Ni_xMn_{3-x}O_4$ correspond to the chemical formulas $Ni_{1.1}Mn_{4.9}O_8$, $Ni_{1.6}Mn_{4.4}O_8$, $Ni_2Mn_4O_8$, and $Ni_{2.4}Mn_{3.6}O_8$, respectively. Very large supercells are required to make the numbers in these chemical formulas be integers, which is computation demanding and complicated. Therefore, three tuned chemical formulas were selected for simplification, which are: $NiMn_5O_8$ ($x = 0.5$), $Ni_2Mn_4O_8$ ($x = 1.0$), and $Ni_3Mn_3O_8$ ($x = 1.5$). Note that the Ni atoms all occupy the B-sites. Therefore, the preference of Ni^{2+} for B-sites is also proven by our computational results, where the B-site occupation in $Ni_xMn_{3-x}O_4$ is energetically more favorable (Figure S20), which is similar to the results of our previous XRD analysis. The DOS demonstrates that pure Mn_3O_4 is a semiconductor and that its band gap is about 1.20 eV (in Figure 5e_{1-1}). Besides the metallic conductivity, $NiMn_5O_8$ ($x = 0.5$) and $Ni_2Mn_4O_8$ ($x = 1.5$) are so-called half-metals, meaning that only spin up electrons are conductive, as shown in Figure 5(e_{2-2} and e_{4-4}). Whereas $Ni_2Mn_4O_8$ ($x = 1.0$) differs slightly around the Fermi level, with the Fermi level crossing the spin-up and spin-down bands (in Figure 5e_{3-3}) , which suggests that ferrimagnetism ($x = 1$) with a similar x value (around 1.0) could make this sample more conductive than the other samples.

Experimental Section

Synthesis of porous $Ni_xMn_{3-x}O_4$@C ($0.55 \leq x \leq 1.2$) nanoparticles

In a typical synthesis, a mixture of $Ni(Ac)\cdot4H_2O$ and $Mn(Ac)\cdot4H_2O$ was dissolved in

95 mL of distilled water. The mixture was incubated in a water-bath at a constant 45 ^{o}C, and after magnetic stirring for 90 min, a light blue transparent liquid was obtained. Meanwhile, citric acid (CA) (0.25 M, 95 mL) was then added into the above mixed solution dropwise, which was generally controlled at about one drop per second. After 2 hours, the temperature was increased from 45 ^{o}C to 85 ^{o}C. Next, the temperature was maintained, and the mixture was stirred overnight until all the water in the container was evaporated. The wet sample was washed and filtered with acetone and ethanol. Then it was dried by using a supercritical dryer, which started at 15 ^{o}C, with the temperature subsequently increased to 38 ^{o}C while flowing CO_2 was injected into the autoclave (corresponding pressure of about 20 MPa and lasting for 5 h). The as-synthesized sample was ground and further annealed with a heating rate of 8 ^{o}C min^{-1} up to the target temperature of 455 ^{o}C, which was maintained for 2.5 h in oxygen atmosphere in a tubular furnace. Finally, a calcination procedure is performed with the given heating rate of 5 ^{o}C min^{-1} up to the target temperature of 650 ^{o}C, which was maintained for 9 h in a tubular furnace under Ar atmosphere with a flow of 80 sccm. In order to change the proportion of nickel (x) in the obtained nanoparticles, different Ni: Mn ratio were designed, yielding porous spinel nanoparticles ($Ni_xMn_{3-x}O_4$@C) with x = 0.55, 0.80, 1.00, 1.20.

For comparison, $Ni_xMn_{3-x}O_4$@C ($x = 0$) was obtained by a similar method to $Ni_xMn_{3-x}O_4$@C ($x = 1$). In order to research whether the Mn^{4+}-rich $Ni_xMn_{3-x}O_4$@C exists in the compounds, $Ni_xMn_{3-x}O_4$@C ($x = 1$) was selected as the study subject (The reason will be given in the paper). The precursor of $Ni_xMn_{3-x}O_4$@C ($x = 1$) was annealed with heating rate of 8 °C min^{-1} at target temperatures of 365, 410, and 500 °C, which were maintained for 2.5 h in oxygen atmosphere in tubular furnace, and the ongoing processes are the same as in the above operations. All of the related chemical reagents are of analytical pure grade and used as received without further purification for all the experiments. Inductively coupled plasma - atomic emission spectroscopy (ICP-AES) was used to confirm the contents of Mn and Ni in the as-prepared samples.

Conclusion

In conclusion, highly porous Mn^{4+}-rich $Ni_xMn_{3-x}O_4$@C ($x = 1$) nano-particles wrapped with an in-situ formed carbon matrix have been successfully fabricated by a facile and eco-friendly method, and the composite has been evaluated as cathode material for an aqueous rechargeable ZIB. In this resulting composite, the substitution of Ni for Mn at the B-sites of Mn_3O_4 was studied by ICP-AES, XPS, XRD, and DFT calculations, which demonstrate that cation-site Ni substitution combined with a high enough doping concentration can decrease the band gap and effectively improve the electronic conductivity in the $Ni_xMn_{3-x}O_4$ crystal structures. Moreover, the highly porous Mn^{4+}-rich structure and amorphous carbon shell leads to fast electron transport and short Zn^{2+} diffusion path in the mild aqueous electrolyte. On the basis of the above unique structure characterizations, the $Ni_xMn_{3-x}O_4$@C ($x = 1$) hybrid display excellent electrochemical properties with outstanding cycling stability, good rate capability and improved zinc storage performance in comparison to most of the reported cathode materials for ZIBs, with high discharge capacities of 139.7 mAh g^{-1} and 98.5 mAh g^{-1} at 50 and 1200 mA g^{-1} respectively, combined with a nearly 93.5% capacity retention at 400 mA g^{-1} after 800 cycles. These exhibited results indicate that our synthesized $Ni_xMn_{3-x}O_4$@C (x = 1) would be a prospective candidate for a remarkable ZIB cathode materials. Furthermore, this work provides some ideas for not only achieving a good understanding of the intercalation process for divalent metal ions (Zn^{2+}, Mg^{2+}, Ca^{2+}), but also facilitating the development of aqueous rechargeable alkalis ion (K^+, Na^+, Li^+) and their aqueous rechargeable hybrid batteries.

Acknowledgements

This work was financially supported by the National Natural Science Foundation of China (No. 21371180) and the Australian Research Council (ARC) (FT150100109 and DP170102406). The authors acknowledge the Partnership for Advanced Computing, which is supported by the National Science Foundation-Centers of Research Excellence in Science and Technology (NSF-CREST Center) for Innovation, Research and Education in Environmental Nanotechnology (CIRE2N) (Grant No. HRD-1736093). This work has been carried out with the support of the China Scholarship Council (CSC No. 201706370175).

Conflict of Interest

The authors declare no conflict of interest.

References

[1] P. Nayak, E. Erickson, F. Schipper, T. Penki, N. Munichandraiah, P. Adelhelm, H. Sclar, F. Amalraj, B. Markovsky, D. Aurbach, *Adv. Energy Mater.,* 2018, **8**, 1702397.

[2] E. Hu, Y., Feng, J. Nai, D. Zhao, Y. Hu, X. Lou, *Energy Environ. Sci.,* 2018, **11**,

872-880.

[3] J. Long, Z. Yang, J. Huang, X. Zeng, *J. Power Sources,* 2017, **359**, 111-118.

[4] a) Y. Liu, Z. Tai, J. Zhang, W. Pang, Q. Zhang, H. Feng, K. Konstantinov, Z. Guo, H. Liu, *Nat. commun.,* 2018, **9**, 3645; b) J. Cuan, Y. Zhou, T. Zhou, S. Ling, K. Rui, Z. Guo, H. Liu, X. Yu, *Adv. Mater.,* 2018, **31**, 1803533; c) Q. Zhang, J. Mao, W. Pang, T. Zheng, V. Sencadas, Y. Chen, Y. Liu, Z. Guo, *Adv. Energy Mater.,* 2018, **8**, 1703288.

[5] J. Long, Z. Yang, Z. Zhang, J. Huang, *J. Electrochem. Soc.,* 2017, **164**, A3068-A3074.

[6] H. Zhang, G. Xia, J. Zhang, D. Sun, Z. Guo, X. Yu, *Adv. Energy Mater.,* 2018, **8**, 1702975.

[7] Y. Fang, X. Yu, X. Lou, *Angew. Chem. Int. Ed.,* 2019, **131**, 1-6.

[8] S. Wang, Y. Fang, X. Wang, X. Lou, *Angew. Chem. Int. Ed.,*2019, **131**, 770-773.

[9] C. Guan, X. Liu, W. Ren, X. Li, C. Cheng, J. Wang, *Adv. Energy Mater.,* 2017, **7**, 1602391.

[10] Y. Huang, M. Zhong, F. Shi, X. Liu, Z. Tang, Y. Wang, Y. Huang, H. Hou, X. Xie, C. Zhi, *Angew. Chem. Int. Ed.,* 2017, **56**, 9141-9145.

[11] J. Yu, W. Lu, J. Smith, K. Booksh, L. Meng, Y. Huang, Q. Li, J. Byun, Y. Oh, Y. Yan, T. Chou, *Adv. Energy Mater.,* 2017, **7**, 1600976.

[12] S. Galliano, F. Bella, G. Piana, G. Giacona, G. Viscardi, C. Gerbaldi, M. Grätzel, C. Barolo, *Sol. Energy,* 2018, **163**, 251-255.

[13] H. Schmies, A. Bergmann, J. Drnec, G. Wang, D. Teschner, S. Kühl, D. Sandbeck,

S. Cherevko, M. Gocyla, M. Shviro, M. Heggen, V. Ramani, R. Dunin-Borkowski, Karl. Mayrhofer, P. Strasser, *Adv. Energy Mater.,* 2018, **8**, 1701663.

[14] F. Rigodanza, L. Đorđević, F. Arcudi, M. Prato, *Angew. Chemie,* 2018, **130**, 5156-5161.

[15] T. Wang, Z. Kou, S. Mu, J. Liu, D. He, I. Amiinu, W. Meng, K. Zhou, Z. Luo, S. Catechumen, F. Verpoort, *Adv. Funct. Mater.,* 2018, **28**, 1705048.

[16] V. Vijayalekshmi, D. Khastgir, *Energy,* 2018, **142**, 313-330.

[17] Q. Yun, Q. Lu, X. Zhang, C. Tan, H. Zhang, *Angew. Chem. Int. Ed.,* 2018, **57**, 626-646.

[18] a) W. Zhang, W. Pang, V. Sencadas, Z. Guo, *Joule*, 2018, **2**, 1534; b) Y. Liu, Z. Tai, T. Zhou, V. Sencadas, J. Zhang, L. Zhang, K. Konstantinov, Z. Guo, H. K. Liu, *Adv. Mater.,* 2017, **29**, 1703028.

[19] W. Li, A. Dolocan, P. Oh, H. Celio, S. Park, J. Cho, A. Manthiram, *Nat. Commun.,* 2017, **8**, 14589.

[20] J. Xu, J. Ma, Q. Fan, S. Guo, S. Dou, *Adv. Mater.,* 2017, **29**, 1606454.

[21] J. Ju, E. Lee, C. Yoon, S. Myung, Y. Sun, *J. Phys. Chem. C,* 2013, **118**, 175-182.

[22] H. Kim, J. Hong, K. Park, H. Kim, S. Kim, K. Kang, *Chem. Rev.,* 2014, **114**, 11788-11827.

[23] H. Xu, X. Zhu, K. Sun, Y. Liu, X. Xie, *Adv. Mater. Inter.,* 2015, **2**, 1500239.

[24] G. Jin, H. Qiao, H. Xie, H. Wang, K. He, P. Liu, J. Chen, Y. Tang, S. Liu, C. Huang, *Electrochim. Acta,* 2014, **150**, 1-7.

[25] J. Tarascon, M. Armand, *Nature,* 2001, **414**, 359.

[26] M. Rahman, A. Glushenkov, T. Ramireddy, Y. Chen, *Chem. Commun.,* 2014, **50**, 5057-5060.

[27] C. Xu, B. Li, H. Du, F. Kang, *Angew. Chem. Int. Ed.,* 2012, **51**, 933-935.

[28] a) Z. Jia, B. Wang, Y. Wang, *Mater. Chem. Phys.,* 2015, **149**, 601-606. b) B. Sambandam, V. Soundharrajan, S. Kim, M. Alfaruqi, J. Jo, S. Kim, V. Mathew, Y. Sun, J. Kim, *J. Mater. Chem. A*, 2018, **6**, 15530-15539. c) B. She, L. Shan, H. Chen, S. Liang, *J. Energy Chem.*, 2019, **37**, 172-175. d) X. Chen, L. Wang, H. Li, F. Cheng, J. Chen, *J. Energy Chem.*, 2019, **38**, 20-25.

[29] B. Zhang, Y. Liu, X. Wu, Y. Yang, Z. Chang, Z. Wen, Y. Wu, *Chem. Commun.,* 2014, **50**, 1209-1211.

[30] G. Li, Z. Yang, Y. Jiang, C. Jin, W. Huang, X. Ding, Y. Huang, *Nano Energy,* 2016, **25**, 211-217.

[31] D. Kundu, S. Vajargah, L. Wan, B. Adams, D. Prendergast, L. Nazar, *Energy Environ. Sci.,* 2018, **11**, 881-892.

[32] M. Alfaruqi, V. Mathew, J. Song, S. Kim, S. Islam, D. Pham, J. Jo, S. Kim, J. Baboo, Z. Xiu, K. Lee, Y. Sun, Jaekook Kim, *Chem. Mater.,* 2017, **29**, 1684-1694.

[33] W. Liu, J. Hao, C. Xu, J. Mou, L. Dong, F. Jiang, Z. Kang, J. Wu, B. Jiang, F. Kang *Chem. Commun.,* 2017, **53**, 6872-6874.

[34] N. Zhang, F. Cheng, Y. Liu, Q. Zhao, K. Lei, C. Chen, X. Liu, J. Chen, *J. Am. Chem. Soc.,* 2016, **138**, 12894-12901.

[35] Z. Liu, G. Pulletikurthi, F. Endres, *ACS Appl. Mater. Inter.,* 2016, **8**, 12158-12164.

[36] L. Zhou, K. Zhang, Z. Hu, Z. Tao, L. Mai, Y. Kang, S. Chou, J. Chen, *Adv. Energy Mater.,* 2018, **8**, 1701415.

[37] H. Kim, D. Seo, H. Kim, I. Park, J. Hong, K. Park, K. Kang, *Chem. Mater.,* 2012, **24**, 720-725.

[38] K. Jurewicz, E. Frackowiak, F. Beguin, *Fuel Process. Technol.,* 2002, **77**, 415-421.

[39] C. Yuan, J. Li, L. Hou, X. Zhang, L. Shen, X. Lou, *Adv. Funct. Mater.,* 2012, **22**, 4592-4597.

[40] P. Hall, M. Mirzaeian, S. Fletcher, F. Sillars, A. Rennie, G. Shitta-Bey, G. Wilson , A. Cruden, R. Carter, *Energy Environ. Sci.,* 2010, **3**, 1238-1251.

[41] H. Nan, W. Ma, Z. Gu, B. Geng, X. Zhang, *RSC Adv.,* 2015, **5**, 24607-24614.

[42] K. Shaikh, S. Warrick, L. Gurung, D. Kwak, J. Bumpus, *Abstracts of Papers of the American Chemical Society*, 2017**, 253**.

[43] X. Lu, W. Bian, Y. Li, H. Zhu, Z. Fu, Q. Zhang, *J. Am. Ceram. Soc.,* 2018, **101**, 1646-1654.

[44] S. Greenwald, S. Pickart, F. Grannis, *J. Chem. Phys.,* 1954, **22**, 1597-1600.

[45] Y. Zhou, S. Sun, J. Song, S. Xi, B. Chen, Y. Du, A. Fisher, F. Cheng, X. Wang, H. Zhang, Z. Xu, *Adv. Mater.,* 2018, **30**, 1802912.

[46] J. Töpfer, A. Feltz, D. Gräf, B. Hackl, L. Raupach, P. Weissbrodt, *Phys. Status Solidi A,* 1992, **134**, 405-415.

[47] J. Huang, H. Hsu, C. Cheng, *J. Magn. Magn. Mater.,* 2014, **149**, 358-359.

[48] H. Jung, S. Lee, D. Lee, K. Kim, *J. Ceram. Process. Res.,* 2016, **17**, 758-762.

[49] Y. Lei, X. Lin, H. Liao, *Sep. Purif. Technol.,* 2018, **192**, 220-229.

[50] M. Muralidharan, P. Rohini, E. Sunny, K. Dayas, A.Seema, *Ceram. Int.,* 2012, **38**,

6481-6486.

[51] C. Pan, R. Nuzzo, A. Gewirth, *Chem. Mater.,* 2017, **29**, 9351-9359.

[52] K. Dokko , M. Mohamedi, N. Anzue , T. Itoh, I. Uchida, *J. Mater. Chem.,* 2002, **12**, 3688-3693.

[53] J. Li S. Xiong, Y. Liu, Z. Ju, Y. Qian, *Nano Energy,* 2013, **2**, 1249-1260.

[54] M. Peck, M. Langell, *Chem. Mater.,* 2012, **24**, 4483-4490.

[55] H. Xia, Y. Wan, F. Yan, L. Lu, *Mater. Chem. Phys.,* 2014, **143**, 720-727.

[56] J. Wang, J. Zhang, *J. Mater. Res.,* 2012, **27**, 928-931.

[57] R. Kalubarme, H. Jadhav, H. Park, *Electrochim. Acta*, 2013, **87**, 457-465.

[58] M. Chigane, M. Ishikawa, *J. Electrochem. Soc.*, 2000, **147**, 2246-2251.

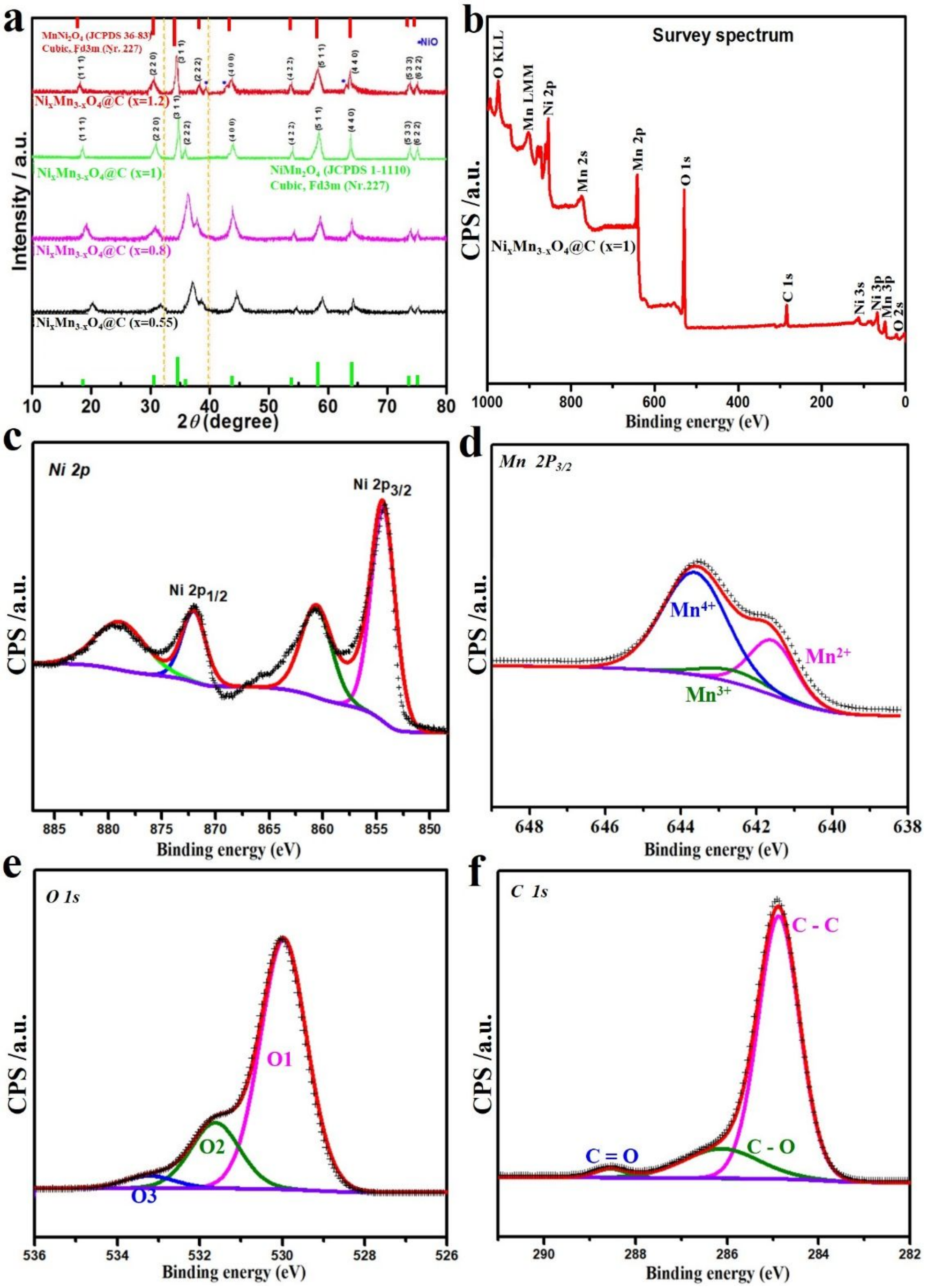

Figure 1. a) XRD patterns for $Ni_xMn_{3-x}O_4$@C samples ($x = 0.55, 0.8, 1.0, 1.2$). b) XPS survey spectrum of $Ni_xMn_{3-x}O_4$@C ($x = 1$). c-f) XPS narrow scan spectra for Ni 2p (c), Mn $2p_{3/2}$ (d), O 1s (e) and C 1s (f) for $Ni_xMn_{3-x}O_4$@C ($x = 1$).

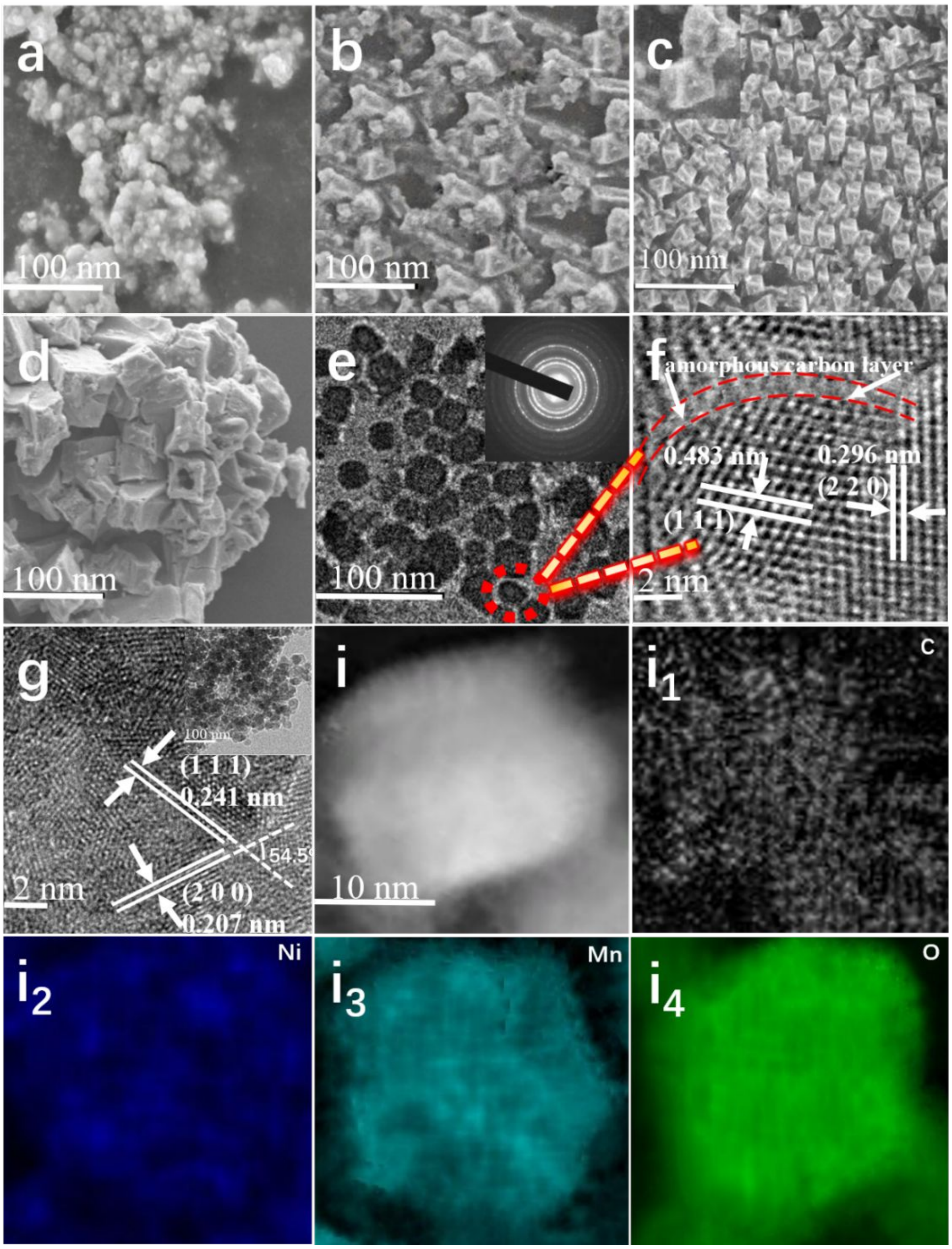

Figure 2. a-d) SEM images of $Ni_xMn_{3-x}O_4$@C samples: $x = 0.55$ (a), $x = 0.8$ (b), $x = 1$ (c), $x = 1.2$ (d). e) TEM image of $Ni_xMn_{3-x}O_4$@C ($x = 1$), (inset: the corresponding SAED pattern. f) HR-TEM image of indicated area in (e). g) HR-TEM image of $Ni_xMn_{3-x}O_4$@C ($x = 1$), with the inset the corresponding low-resolution TEM image. i) Scanning TEM (STEM) image of a $Ni_xMn_{3-x}O_4$@C ($x = 1$) nanoparticle, with (i_1-i_4) the corresponding EDX elemental maps of C (i_1), Ni (i_2), Mn (i_3), and O (i_4).

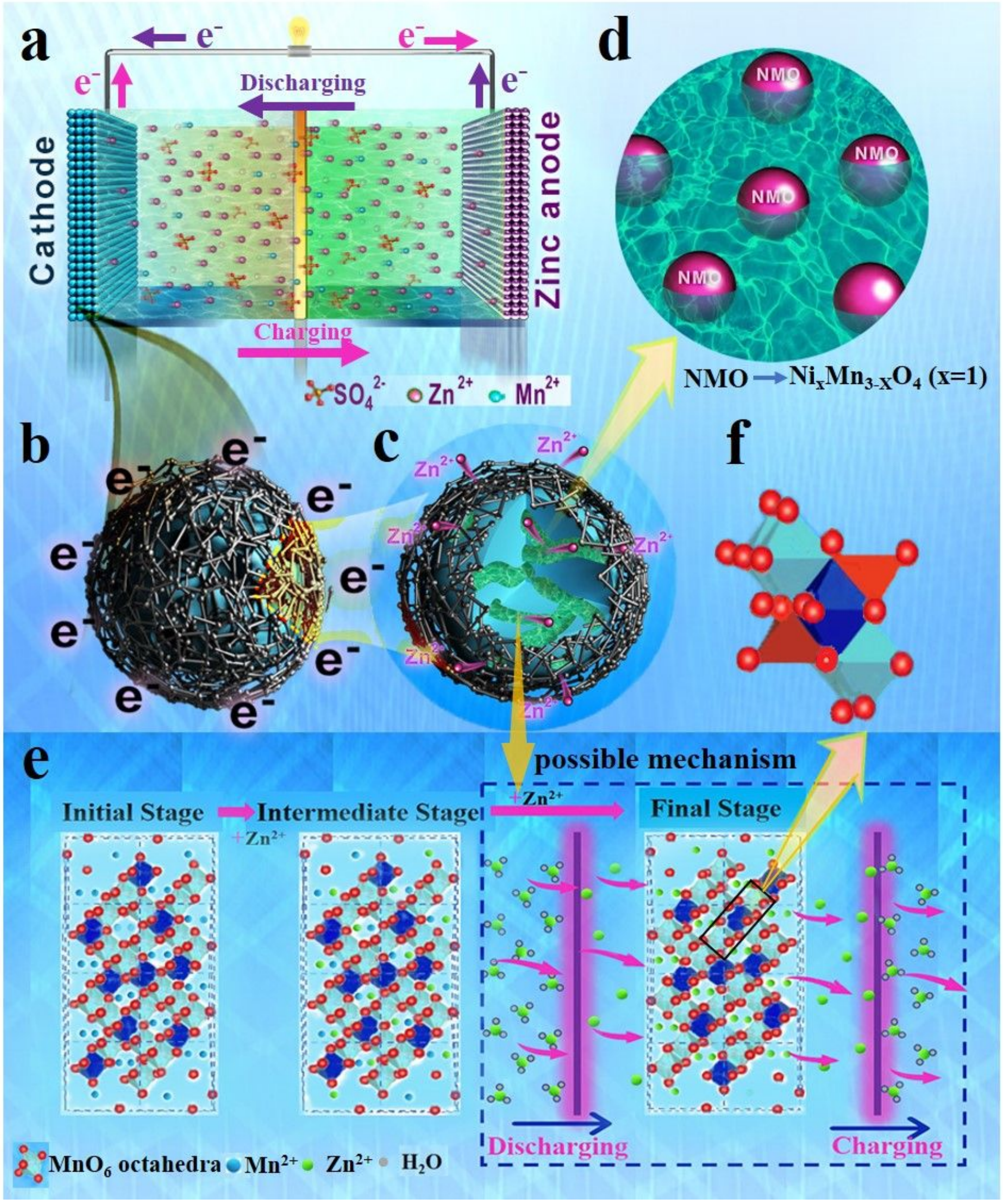

Figure 3. a-b) Schematic illustration of ZIB comprising $Ni_xMn_{3-x}O_4$@C ($x = 1$) cathode, battery separator and zinc anode, as well as partial enlargement area of the cathode material. c-d) Enlargement of the interior of $Ni_xMn_{3-x}O_4$@C ($x = 1$) particles, with the $Ni_xMn_{3-x}O_4$ inside the nano-particles generating numerous tunnels so that Zn^{2+} could transfer more efficiently through these tunnels. e) Schematic illustration of the reaction pathways of zinc ion intercalation/deintercalation into/from the $Ni_xMn_{3-x}O_4$@C (x = 1) electrode. f) Basic unit of the $Ni_xMn_{3-x}O_4$ spinel structure.

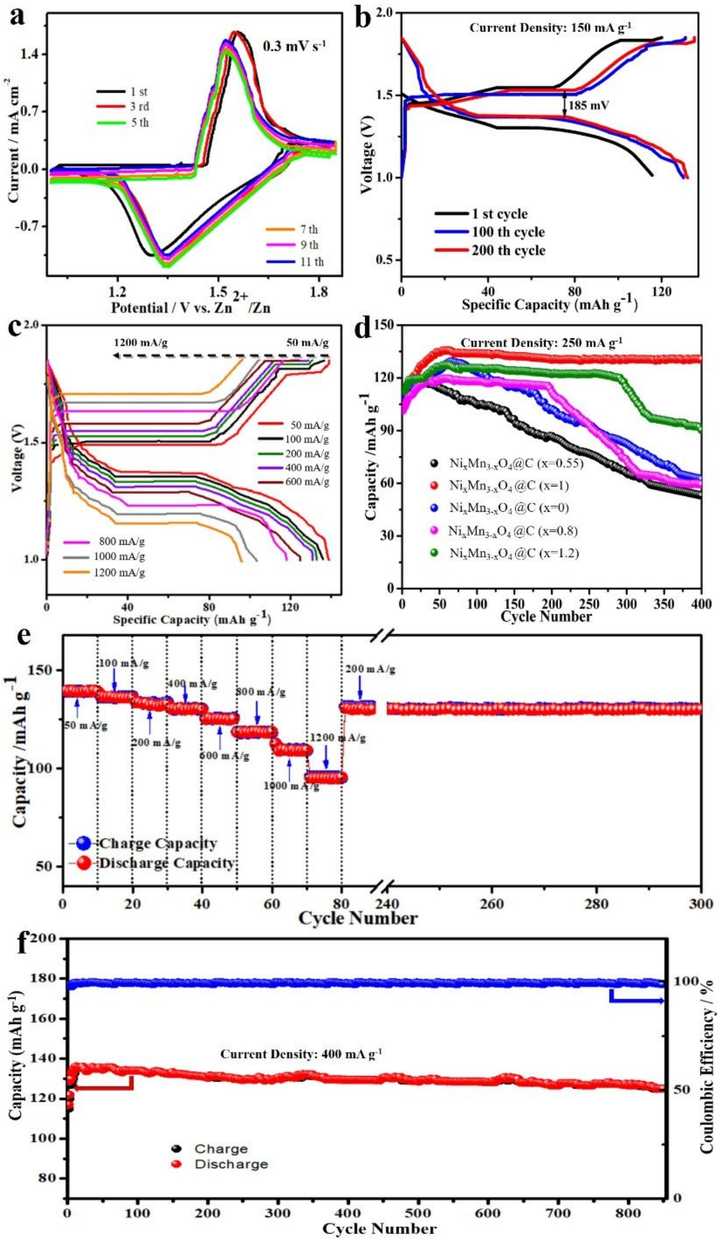

Figure 4. a) CV curves of $Ni_xMn_{3-x}O_4$@C ($x = 1$) measured within the first eleven cycles at a scan rate of 0.3 mV s^{-1}. b) Charge-discharge voltage curves for selected cycles of the electrode at 150 mA g^{-1}. c) Charge-discharge profiles of $Ni_xMn_{3-x}O_4$@C ($x = 1$) at different rates. d) Cycling performances of $Ni_xMn_{3-x}O_4$@C (x = 0, 0.55, 0.8, 1, 1.2) samples at 250 mA g^{-1}. e) Rate capability of $Ni_xMn_{3-x}O_4$@C ($x = 1$) electrode and its cycling performance after rate tests at 200 mA g^{-1}. f) Cycling performance and coulombic efficiency of $Ni_xMn_{3-x}O_4$@C ($x = 1$) at 400 mA g^{-1} over 850 cycles.

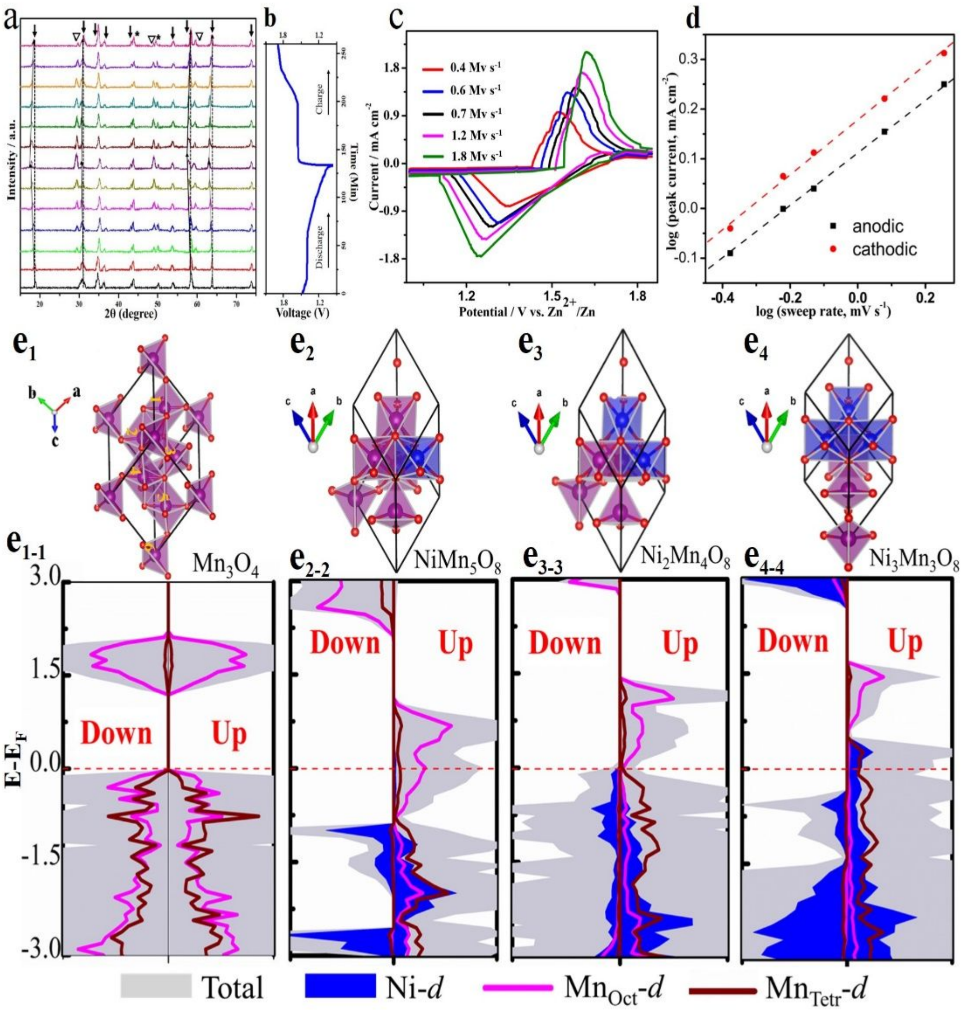

Figure 5. a) Ex-situ XRD patterns of the $Ni_xMn_{3-x}O_4$@C ($x = 1$) cathode for the zinc ion batteries during discharging/charging; ∗ stainless steel current collector, ↓ $Ni_xMn_{3-x}O_4$@C ($x = 1$), ∇$(Zn_{0.988}Mn_{0.012})(Mn_{1.326}Zn_{0.024}Ni_{0.65})O_4$. b) Corresponding voltage-time curves. c) CVs collected at various scan rates. d) Log *i* vs. log *v* plots at specific peak currents. e$_1$-e$_4$) Structures of pure Mn_3O_4 and $Ni_xMn_{3-x}O_4$: e$_1$-e$_4$) Primitive cells of (e$_1$) Mn_3O_4 with space group I41/amd, (e$_2$) $NiMn_5O_8$, (e$_3$) $Ni_2Mn_4O_8$, and (e$_4$) $Ni_3Mn_3O_8$ based on the primitive cell of Mn_3O_4 by replacing octahedrally-coordinated Mn atoms. e$_{1-1}$-e$_{4-4}$) Partial density of states (PDOS) of pure Mn_3O_4 (e$_{1-1}$), $NiMn_5O_8$ (e$_{2-2}$), $Ni_2Mn_4O_8$ (e$_{3-3}$), and $Ni_3Mn_3O_8$ (e$_{4-4}$); the grey area shows the total DOS, and the other colours indicate the *d* orbitals of the transition metals.